*Advanced Science*

ADVANCED SCIENCE Open Access

www.advancedscience.com

RESEARCH ARTICLE OPEN ACCESS

# Correlated Charge Order Intertwined With Time-Reversal Symmetry-Breaking Nodal Superconductivity in the Kagome Superconductor $CeRu_3Si_2$

O. Gerguri[1,2] | P. Kral[1] | M. Spitaler[1,3] | M. Salamin[4] | J.N. Graham[1] | A. Doll[1] | I. Biało[1,2] | I. Plokhikh[5,6] | J.A. Krieger[1] | T. J. Hicken[1] | J. Oppliger[2] | L. Martinelli[2] | A. Steppke[1] | N. Shepelin[1] | R. Khasanov[1] | M.v. Zimmermann[7] | B. Monserrat[8] | H. Luetkens[1,3] | J. Chang[2] | F.O. von Rohr[3,4] | Sun-Woo Kim[8,9] | Z. Guguchia[1,3]

[1]PSI Center for Neutron and Muon Sciences CNM, Villigen PSI, Switzerland | [2]Physik-Institut, Universität Zürich, Zürich, Switzerland | [3]National Centre of Competence in Research Muoniverse, Switzerland | [4]Department of Quantum Matter Physics, University of Geneva, Geneva, Switzerland | [5]Department of Physics, TU Dortmund University, Dortmund, Germany | [6]Research Center Future Energy Materials and Systems (RC FEMS), Dortmund, Germany | [7]Deutsches Elektronen-Synchrotron DESY, Hamburg, Germany | [8]Department of Materials Science and Metallurgy, University of Cambridge, Cambridge, United Kingdom | [9]Department of Physics, Hanyang University, Seoul, Republic of Korea

**Correspondence:** Sun-Woo Kim (kimsunwoo821@gmail.com) | Z. Guguchia (zurab.guguchia@psi.ch)

**Received:** 14 June 2026 | **Revised:** 28 September 2026 | **Accepted:** 30 October 2026

**Keywords:** charge order | condensed matter physics | magnetoresistance | muon spin spectroscopy | superconductivity | time-reversal symmetry-breaking

## ABSTRACT

Kagome materials provide a platform for exploring flat-band-driven symmetry-breaking quantum states. Here, we introduce $CeRu_3Si_2$, a kagome superconductor in which our first-principles calculations show the coexistence of Ru $d$-orbital kagome flat bands and flat bands derived from $Ce^{4+}4f$-states. X-ray diffraction reveals a dominant 1/2 charge order with a much weaker 1/3 component persisting up to room temperature. Deep within the charge-ordered state, magnetoresistance emerges below 80 K and strengthens further below 30 K. Zero-field muon spin-rotation measurements show no time-reversal symmetry (TRS) breaking in the normal state, in contrast to $LaRu_3Si_2$ and $YRu_3Si_2$. However, an applied magnetic field induces weak magnetism. Across the $ARu_3Si_2$ family ($A$=La, Y, Ce), the superconducting transition temperature $T_c$ scales linearly with the onset temperature of normal-state TRS breaking $T_{TRSB}$ and the magnitude of the field-induced magnetic response, revealing a direct positive correlation between normal-state symmetry breaking and superconductivity. Furthermore, we identify that $CeRu_3Si_2$ is the first 132-type kagome compound to host nodal superconductivity together with spontaneous internal magnetic fields, suggestive of intrinsic TRS breaking in the superconducting state. These results establish $CeRu_3Si_2$ as a unique platform where kagome-derived $d$- and $f$-electron flat bands coexist with rich hierarchy of electronic orders.

## 1 | Main

The interplay between crystal structure and electron correlations gives rise to a wide range of emergent electronic phases. Kagome lattices are a prime platform, hosting van Hove singularities [1–4], flat bands [5–10], Dirac fermions [9, 11], pair density waves [12], unconventional superconductivity [7, 13], and time-reversal symmetry breaking (TRSB) [7, 13–17]. A prominent example is the ternary kagome family $ARu_3Si_2$ ($A$ = La, Y). $LaRu_3Si_2$ [6, 18–22] exhibits a dome-shaped superconducting phase diagram with

O. Gerguri and P. Kral contributed equally to the work.

This is an open access article under the terms of the Creative Commons Attribution License, which permits use, distribution and reproduction in any medium, provided the original work is properly cited.
© 2026 The Author(s). *Advanced Science* published by Wiley-VCH GmbH

one of the highest $T_c$ values among kagome superconductors under low pressure, alongside multiple charge orders, field-induced magnetism below 80 K, and TRSB [16] below 35 K. Substituting Y for La introduces chemical pressure, lowering $T_c$ to ~3.4 K while strengthening charge order; $YRu_3Si_2$ [23] also shows TRSB below 25 K and field-induced magnetism below 90 K. Despite differing energy scales, both compounds share nodeless superconductivity, high-temperature charge order, magnetoresistance, and normal-state TRSB. These phenomena arise from a common electronic structure with kagome-derived flat bands of Ru $d$-electrons, underscoring the central role of flat-band-driven correlations in shaping their phase diagrams.

In the above-mentioned and other kagome materials, attention has so far focused almost exclusively on $d$-electron flat bands. A fundamental open question is whether qualitatively new physics can arise when flat bands of distinct origin–such as kagome $d$-electron and $f$-electron states–interact within a single system. To address this, we investigate the role of incorporating $f$-electron degrees of freedom by focusing on $CeRu_3Si_2$, in which the superconducting transition temperature is further reduced to $T_c \sim$ 1 K. Previous investigations [24–29] of $CeRu_3Si_2$ have been largely restricted to bulk measurements, such as magnetic susceptibility and specific heat. As a result, the electronic structure, the contribution of Ce $4f$ electrons to the density of states, the superconducting gap symmetry, and the possible emergence of charge order or anomalous normal-state electronic responses have remained under-explored. Here, our central goal is to elucidate how the strong suppression of $T_c$ correlates with changes in the normal-state properties, to determine whether Ce $4f$ electrons contribute magnetically or via electronic correlations related to flat-bands. This would help to establish whether a fundamental link exists between superconductivity and normal-state electronic responses across the kagome family $ARu_3Si_2$ ($A$ = La, Y, and Ce). Details regarding growth method and phase purity determination of $CeRu_3Si_2$ samples are found in Section S1/ Figure S1. In this work, we present a comprehensive study of $CeRu_3Si_2$ over a wide temperature range, combining single crystal X-ray diffraction (XRD), magnetotransport, $\mu$SR, and first-principles calculations to uncover the rich landscape of electronic phases and to elucidate the influence of both $f$-electron and kagome $d$-electron flat bands on the superconducting and normal-state properties.

## 2 | Results and Discussion

### 2.1 | Correlated Charge Orders Revealed by X-Ray Diffraction and DFT Calculations

Firstly, to determine the presence of charge order, a synchrotron [30] X-ray diffraction (XRD) experiments on $CeRu_3Si_2$ were conducted over a temperature range of 10–300 K. The reconstructed reciprocal patterns along the (H K 8) diffraction plane, obtained at various temperatures are shown in Figure 1a–f. From 300 K down to 10 K, 1/2 ($q_1$ = (1/2, 0, 0), $q_2$ = (1/2, 1/2, 0) and $q_3$ = (1/2, -1/2, 0)) and 1/3 ($q_1$ = (1/3, 0, 0), $q_2$ = (1/3, 1/3, 0) and $q_3$ = (1/3, -1/3, 0)) superstructure reflections emerge. The reciprocal vectors are given relative to the a×a×2c unit cell, according to the notation in Ref. [18]. This establishes the presence of various charge ordering within the orthorhombic phase in $CeRu_3Si_2$ at least below 300 K (for additional information, refer to Section S2/Figure S2). Although in the current work, we did not explore the temperature region above 300 K, the direct siblings of $CeRu_3Si_2$, the $RRu_3Si_2$ phases, undergo a transformation from a high-temperature $P6/mmm$ to low-temperature orthorhombic phases at temperature as high as 600 K for $R$ = La [16, 18], 760 K for $R$ = Nd [31] and over 800 K for $R$ = Y [23]. The observation of all three symmetry-related arms of charge-order vectors as well as pseudo-hexagonal symmetry of the diffraction pattern are due to the formation of three orthorhombic domains oriented according to $C_3$ symmetry of the high-temperature $P6/mmm$ phase ($a\times a\times c$) rather than 3$q$ order. Similar to $YRu_3Si_2$ and (Nd/Pr)$Ru_3Si_2$, the 1/2 order can be described within the $Pmma$ space group. The instability of the $P6/mmm$ phase and its tendency to transform into low-temperature, lower-symmetry (orthorhombic) structures is further supported by DFT calculations.

To gain deeper insight into the charge-ordered states in $CeRu_3Si_2$, we performed first-principles DFT calculations (Figure 2). Note that the crystal structures shown in Figure 2 are obtained from first-principles calculations. These calculations reveal several key features of the electronic structure. In particular, they show the coexistence of Ru $d$-orbital kagome flat bands and flat bands originating from the $Ce^{4+}4f$ states, with the Fermi level located between these two sets of bands (Figure 2b). The $f$ orbitals form flat bands situated above the Fermi level, consistent with a $4f^0$ configuration. The corresponding phonon dispersion shows multiple imaginary modes in the $q_z = 1/2$ plane (Figure 2c), which leads to two competing charge-order patterns: a $q = 1/2$ $Pmma$ charge order (CO) and a $q = 1/3$ charge order with $Imma$ symmetry (CO-II), as displayed in Figure 2d,e. The CO structure exhibits a stripe-like pattern of in-plane Ru atoms while the CO-II structure shows a corner-sharing Star-of-David pattern. These distortions are accompanied by a suppression of density of states near the Fermi level associated with the in-plane Ru $d_{xy}$ and $d_{x^2-y^2}$ orbitals that comprise the Ru-$d$ flat bands (Figure 2f). We also find that the Ce-$f$ flat bands shift upward upon the formation of the charge ordered states. These results show that charge-order formation is accompanied by pronounced changes in both the Ru-$d$ and Ce-$4f$ electronic states.

Further analysis reveals that the Ce-$4f$ states play a crucial role in determining the charge-ordered ground state of this compound (Figure 2g), despite the Ce $4f$ flat bands lying above the Fermi level. While the Hubbard interaction $U$ on the Ce $4f$ orbitals has only a minor influence on the lattice parameters (less than 0.4% change from $U = 0$ to 9 eV), it strongly reshapes the structural energy landscape associated with charge order. This strong dependence demonstrates that the static local correlations described by DFT+$U$ are essential for stabilizing the experimentally observed CO ground state and reproducing the energetic hierarchy of the charge-ordered structures (see Section S3/Figure S4, Table S1–4). Specifically, when the Ce $4f$ electrons are excluded from the valence (i.e., treated as core states), CO-II cannot be stabilized even as a metastable structure. Moreover, CO is not obtained as the lowest energy ground state but instead lies 1.2 meV/f.u. above the CO* structure with $q = 1/4$. The resulting prediction of an unobserved $q = 1/4$ ground state is inconsistent with experiment.

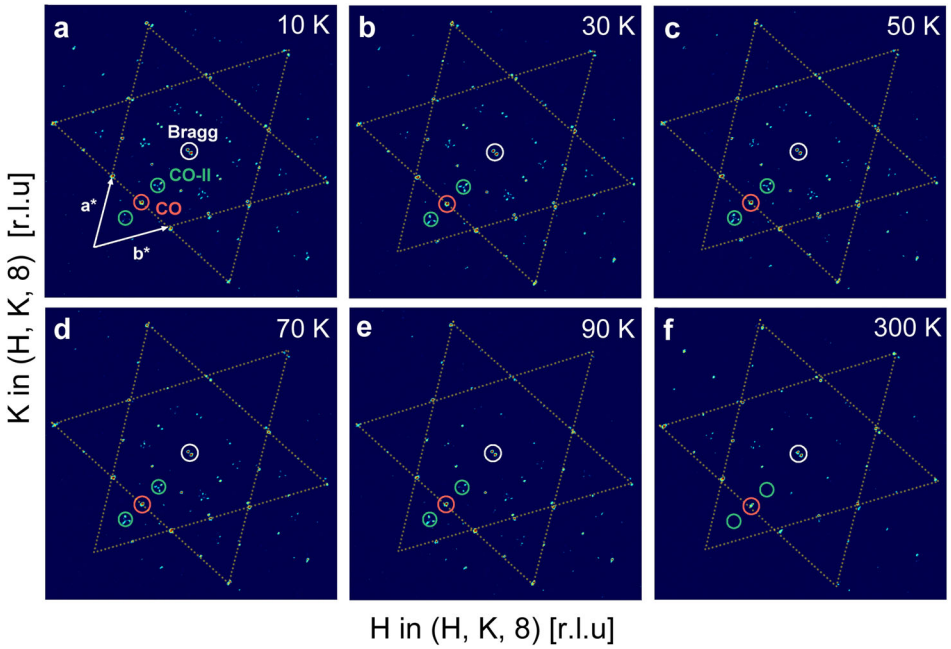


**FIGURE 1** | Synchrotron X-ray diffraction experiments on a single crystal of $CeRu_3Si_2$. (a–f) Reconstructed reciprocal space along the (H, K)- plane at fixed L = 8 r.l.u (reciprocal lattice units), obtained at various temperatures between 10 and 300 K. The main reflections are split, due to the formation of orthorhombic domains. Arrows indicate the reciprocal lattice vectors. White, red and green circles mark the Bragg peak, primary charge order CO peak, and the secondary charge order CO-II peak, respectively.

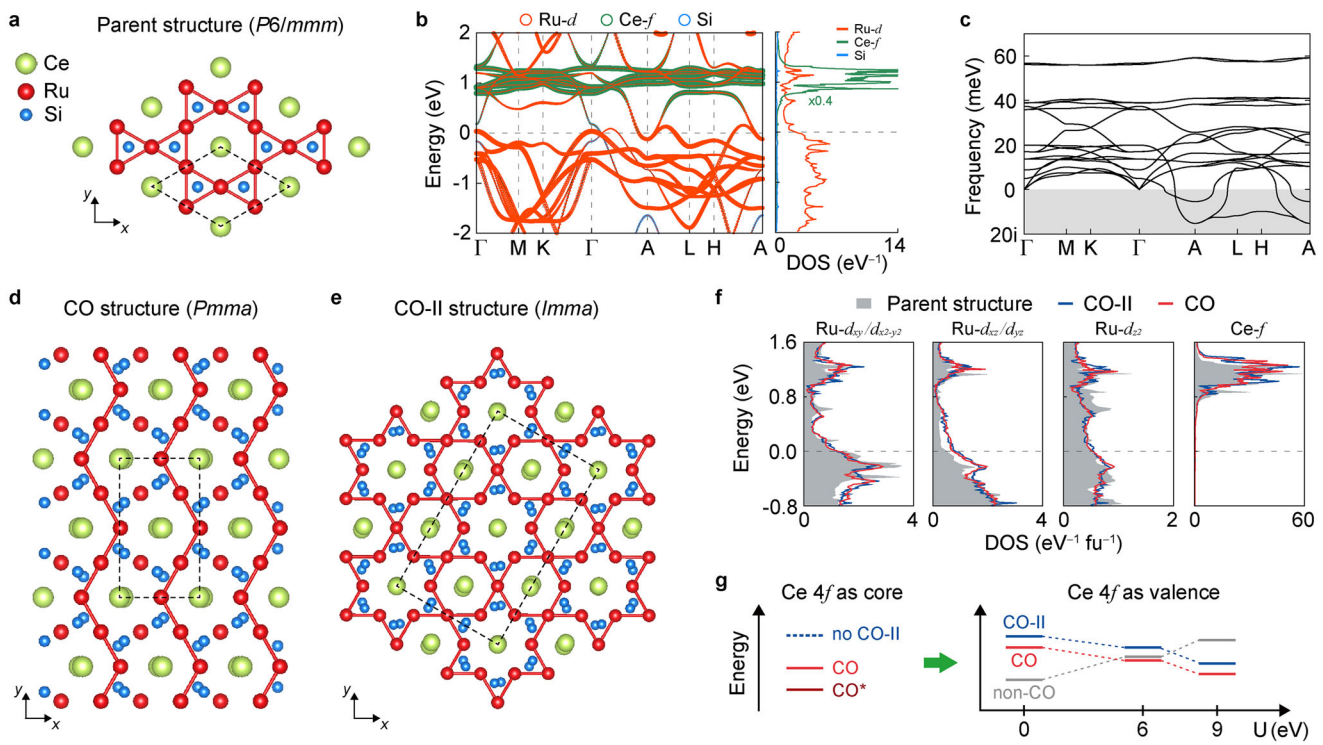


**FIGURE 2** | Correlated charge-ordered states in $CeRu_3Si_2$. (a) Atomic structure of the parent phase ($P6/mmm$). The dashed line indicates the primitive unit cell. (b) Orbital-projected band structure and density of states (DOS) of the parent structure. The sizes of the differently colored open circles overlaid on the band structure are proportional to the orbital-projected weights of the corresponding band states. (c) Phonon dispersion of the parent structure. (d,e) Atomic structures of the CO ($Pmma$) (d) and CO-II ($Imma$) (e) phases. The atomic structures shown in (a), (d), and (e) were obtained from first-principles calculations. (f) Orbital-projected DOS for the three structures. (g) Schematic energy diagram of the CO states obtained by treating the Ce 4$f$ electrons as core states (left) and as valence states (right). In the left panel, CO-II cannot be stabilized and instead relaxes into a different distorted structure, while CO$^*$ denotes a charge order with $q = 1/4$. In the right panel, the relative energies of CO, CO-II, and non-CO are shown as a function of the Hubbard $U$ on the Ce 4$f$ orbitals. Non-CO denotes a distorted structure with negligible Ru distortions. Numerical values of the relative energies are provided in Table S1.

In contrast, when the Ce 4$f$ electrons are included as valence states, both CO and CO-II can be stabilized. At $U = 0$, however, a non-CO structure with negligible Ru distortions remains the ground state, lying 23.1 and 25.1 meV/f.u. below CO and CO-II, respectively. At $U = 6$ eV, CO and non-CO become nearly degenerate, with an energy difference of only 0.1 meV/f.u., while CO-II lies 4.7 meV/f.u. above CO. At $U = 9$ eV, the experimentally dominant CO structure becomes the clear ground state, with CO-II and non-CO lying 6.8 and 22.7 meV/f.u. higher, respectively. Thus, a sufficiently large on-site interaction, as represented by $U = 9$ eV, reproduces the experimentally observed hierarchy consisting of a dominant CO state and a higher-energy competing CO-II state. Taken together, the electronic-structure changes and the strong dependence of the charge-order energetics on the treatment of the Ce-4$f$ electrons demonstrate that both the Ru-$d$ and Ce-4$f$ sectors participate in the formation of the charge-ordered states. These results also highlight the correlated nature of the dominant CO state, in the sense that its stability and relative energetics depend critically on the static local Ce-4$f$ correlations captured within DFT+$U$. Establishing whether electronic correlations are the primary microscopic driving mechanism of the charge order will require more advanced many-body calculations and/or additional direct experimental evidence beyond the scope of the present work.

## 2.2 | Magnetoresistance, Hall Reversal, and Superconducting Properties

Having established the presence of correlated charge order and supported it by DFT calculations, we now examine the transport properties in both the normal and superconducting states. Figure 3a shows the temperature dependence of the electrical resistivity of $CeRu_3Si_2$ above $T_c$. In the charge-ordered phase, the resistivity remains metallic, consistent with behavior reported for $LaRu_3Si_2$ [16], $YRu_3Si_2$ [23], and the kagome superconductors $AV_3Sb_5$ [32, 33]. This indicates that charge ordering in $CeRu_3Si_2$ only induces a partial reconstruction of the Fermi surface, leaving a substantial fraction of itinerant carriers intact. Electrical transport is dominated by ungapped bands, resulting in metallic behavior upon cooling. This is typical of multiband or three-dimensional systems [34] and contrasts with quasi-one-dimensional Peierls systems, where charge order [35] opens a large gap and suppresses conductivity. The resistivity curve $\rho(T)$ (Figure 3a) reveals two characteristic temperature scales governing the normal-state electronic properties. The first derivative of $\rho(T)$ (Figure 3b) exhibits a weak anomaly at $T^*_{MR,1} \simeq$ 80 K, followed by a pronounced maximum at $T^*_{MR,2} \simeq$ 30 K. Motivated by these features, we carried out systematic measurements of the magnetoresistance (MR) (Figure 3b,d) (furthermore see Section S3/ Figure S5) and Hall resistivity (Figure 3c) over a broad range of temperatures and magnetic fields. The MR at 14 T enhances below $\simeq$ 80 K and reaches a saturation value up to $\simeq$ 18% at low temperatures, consistent with the positive MR expected in metallic systems [36]. Two clear slope changes can be discerned: an initial onset below $T^*_{MR,1}$ and a much steeper increase below $T^*_{MR,2}$, closely tracking the anomalies in the resistivity derivative. Concurrently, the Hall resistivity undergoes a sign change across $T^*_{MR,1}$. Taken together, these magnetotransport signatures point to a normal-state transition or crossover occurring between the onset of charge order and the emergence of superconductivity.

Figure 3e shows the superconducting transitions under applied magnetic fields. For completeness, the data are also presented as a color map (Figure 3f) with temperature on the horizontal axis and magnetic field on the vertical axis, where blue denotes the zero-resistance superconducting state and red the normal state. The superconducting state is expected to be progressively suppressed by a magnetic field as noted by the shift to lower transition temperatures (see Figure 3e,f), yielding an estimated upper critical field $H_{c2}$ of 1 T at 0.6 K. The transition exhibits an onset at 2 K, while zero resistance is achieved only below 0.9 K, resulting in an unusually broad temperature interval without zero resistance. X-ray diffraction confirms a homogeneous single phase, excluding sample inhomogeneity as the origin of this behavior. Moreover, as shown below in Figure 6d, $\mu$SR detects the onset of superconductivity only below 0.9 K. Given its high sensitivity even to small superconducting volume fractions, this rules out a distribution of transition temperatures, which would otherwise produce a higher-temperature onset. Possible scenarios include the onset of two-dimensional superconducting correlations [37] or spatially decoupled filamentary superconducting regions. However, without measurements on single crystals, it remains difficult to unambiguously establish the presence of two-dimensional superconducting correlations.

## 2.3 | Nodal TRS-Breaking Superconductivity and Scaling Between Superconducting and Normal-State Symmetry Breaking

Next, we present $\mu$SR results that investigate the normal state of $CeRu_3Si_2$. A central question is whether magnetism is associated with the characteristic temperature scales $T^*_{MR,1}$ and $T^*_{MR,2}$ identified in transport, as previously observed in $LaRu_3Si_2$ and $YRu_3Si_2$. To address this issue, we combine zero-field (ZF) and high transverse-field (HTF) $\mu$SR measurements (see Sections S6, S7, S8). The ZF-$\mu$SR spectra display only a very weak depolarization of the muon spin ensemble (Figure 4a), providing no evidence for long-range magnetic order in $CeRu_3Si_2$. Full muon polarization is recovered upon application of a small longitudinal field ($B_{LF} = 5$ mT), indicating that the relaxation originates from weak, internal fields quasi-static on the microsecond timescale. The data are well described by a Gaussian Kubo–Toyabe function (see Section S6/ Equation S1), consistent with previous reports. Importantly, the relaxation rate remains temperature independent down to 1.3 K (Figure 4b), excluding time-reversal symmetry (TRS) breaking across both $T^*_{MR,1}$ and $T^*_{MR,2}$. This demonstrates that the normal state of $CeRu_3Si_2$ preserves TRS, in contrast to its La and Y counterparts (Figure 4b)[16, 23].

To further corroborate these findings, we performed a comprehensive set of HTF-$\mu$SR measurements [38] as seen in Figure 4c and d. At the lowest applied field of 0.01 T, $\sigma_{HTF}$ remains nearly temperature independent down to 3 K, consistent with the ZF-$\mu$SR results. With increasing magnetic field, however, a clear two-step enhancement of $\sigma_{HTF}$ emerges, with onsets at $T^*_{\mu SR,1}$ and a further increase below $T^*_{\mu SR,2}$, demonstrating a field-induced magnetic response that strengthens with field. Notably, the relaxation rate increases across the entire sample volum, which confirms the bulk nature of the magnetic response (see Section S8/ Figure S7). These results establish that the

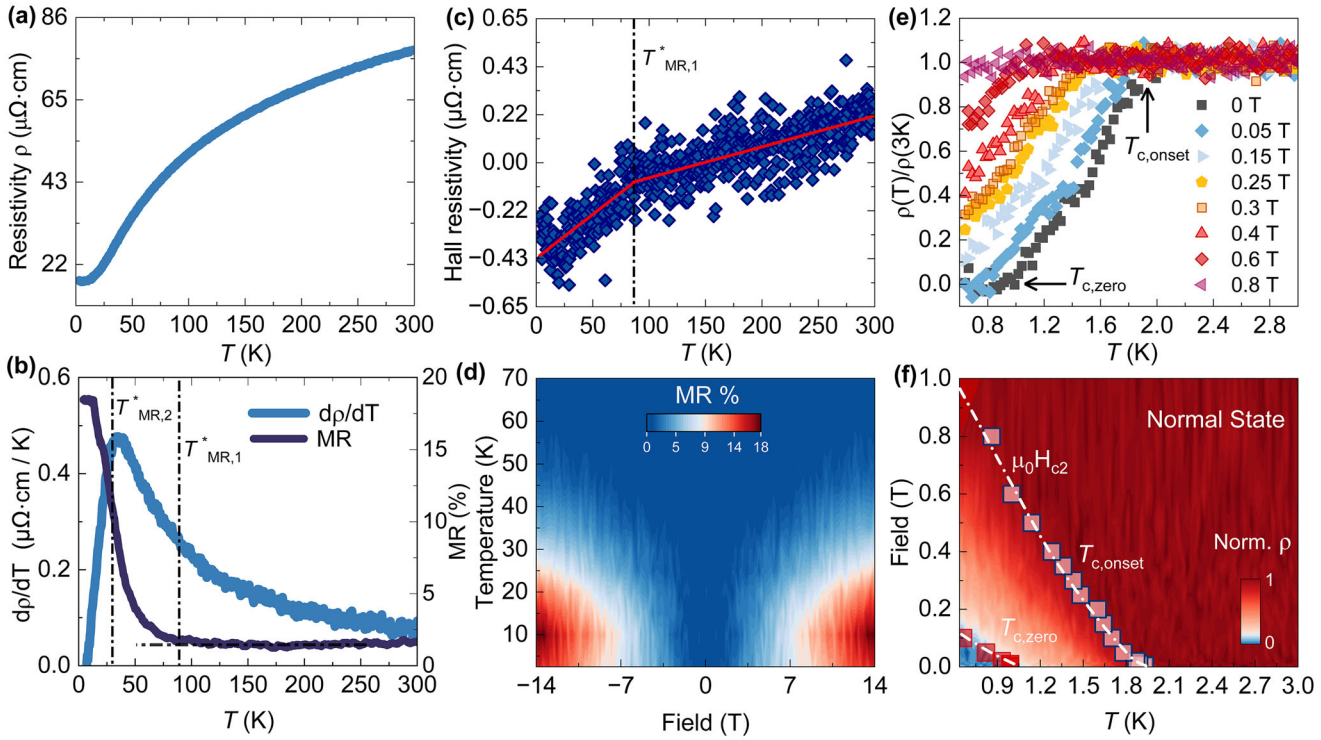


**FIGURE 3** | Magnetotransport experiments on $CeRu_3Si_2$. (a–c) Temperature dependence of the normal state resistivity $\rho$ (a), its first derivative ($d\rho/dT$, left axis) and magnetoresistance (MR, right axis) (b), and Hall resistivity measured at 14 T (c). Dashed vertical lines mark two characteristic temperatures, $T^*_{MR,1}$ and $T^*_{MR,2}$. $T^*_{MR,1}$ corresponds to the onset of magnetoresistance and the sign reversal of the Hall effect, while $T^*_{MR,2}$ marks the peak in $d\rho/dT$. (d) Color plot of the normal state MR, drawn as a function of temperature and applied field (up to 14 T). (e) Temperature dependence of the resistivity across the superconducting transition, measured down to 0.6 K under magnetic fields up to 0.8 T. Arrows indicate temperatures corresponding to the onset of the superconducting transition and the zero-resistance state. (f) Field–temperature color map of the resistivity derived from the data in (e). Pink squares indicate the estimated onset of the superconducting transition, $T_{c,onset}$, while red squares mark the zero-resistance superconducting state at $T_{c,zero}$. Dashed lines are guides to the eye.

magnetoresistance observed in $CeRu_3Si_2$ is associated with a weak, field-induced magnetic state. The absolute increase in relaxation rate, $\Delta\sigma_{HTF} = \sigma_{HTF}(3K) - \sigma_{HTF}(230K)$, amounts to 0.053 $\mu s^{-1}$, significantly smaller than in $LaRu_3Si_2$ and $YRu_3Si_2$. Thus, $CeRu_3Si_2$ is distinguished not only by its reduced superconducting transition temperature $T_c$, but also by the absence of normal-state TRS breaking in zero field and by a substantially weaker field-induced magnetic response. To quantify this trend, we compare $T_c$ with both the onset temperature of ZF-TRS breaking (Figure 5a) and $\Delta\sigma_{HTF}$ measured at 6 and 8 T (Figure 5b) across the $ARu_3Si_2$ series ($A$ = Ce, Y, La). Strikingly, $T_c$ exhibits an approximately linear correlation with both quantities. Although the limited number of compounds currently available within the $ARu_3Si_2$ family precludes establishing a statistically robust universal scaling, the observed correlation between $T_c$ and $T_{TRSB}$ is nevertheless suggestive. Notably, it extends across the presently accessible $T_c$ range of approximately 1–7 K and is accompanied by a systematic correlation between $T_c$ and the magnitude of the field-induced relaxation rate. The concurrent evolution of these two independent measures of the symmetry-breaking response with $T_c$ points to a possible connection between normal-state symmetry breaking and superconductivity. Together, these observations suggest a common underlying electronic mechanism linking symmetry breaking and superconducting pairing within this kagome family. Further studies, particularly systematic tuning across the $Ce_{1-x}La_xRu_3Si_2$ series, will be important to establish whether this correlation represents a more general relationship or instead reflects material-specific effects.

In the following, we investigate the microscopic nature of the superconducting state in $CeRu_3Si_2$. Figure 6a shows representative transverse-field (TF) $\mu$SR time spectra recorded in an applied magnetic field of 10 mT above ($T$ = 1.6 K) and below ($T$ = 0.25 K) the superconducting transition. Above $T_c$, the muon spin precession exhibits only weak damping, arising from the random local fields of nuclear moments. Upon entering the superconducting state, the damping rate increases markedly, reflecting the formation of a non-uniform internal magnetic field distribution associated with a flux-line lattice [39]. This evolution is further illustrated in Figure 6b, which displays the Fourier transforms of the $\mu$SR spectra at the corresponding temperatures. Above $T_c$, a sharp and symmetric field distribution is observed. In contrast, in the superconducting state the distribution becomes significantly broadened and asymmetric, and shifts relative to the applied field–hallmarks of a vortex lattice in the mixed state. From these data, two key quantities are extracted: the diamagnetic shift $\Delta B_{int} = \mu_0(H_{int,SC} - H_{int,NS})$, defined as the difference between the internal fields in the superconducting $H_{int,SC}$ and normal states $H_{int,NS}$ and the total muon spin depolarization rate $\sigma_{tot}$ ($= \sqrt{\sigma_{sc}^2 + \sigma_{nm}^2}$), which includes contributions from the superconducting vortex lattice ($\sigma_{sc}$) and from nuclear dipolar fields ($\sigma_{nm}$) dominant in the normal state. The temperature

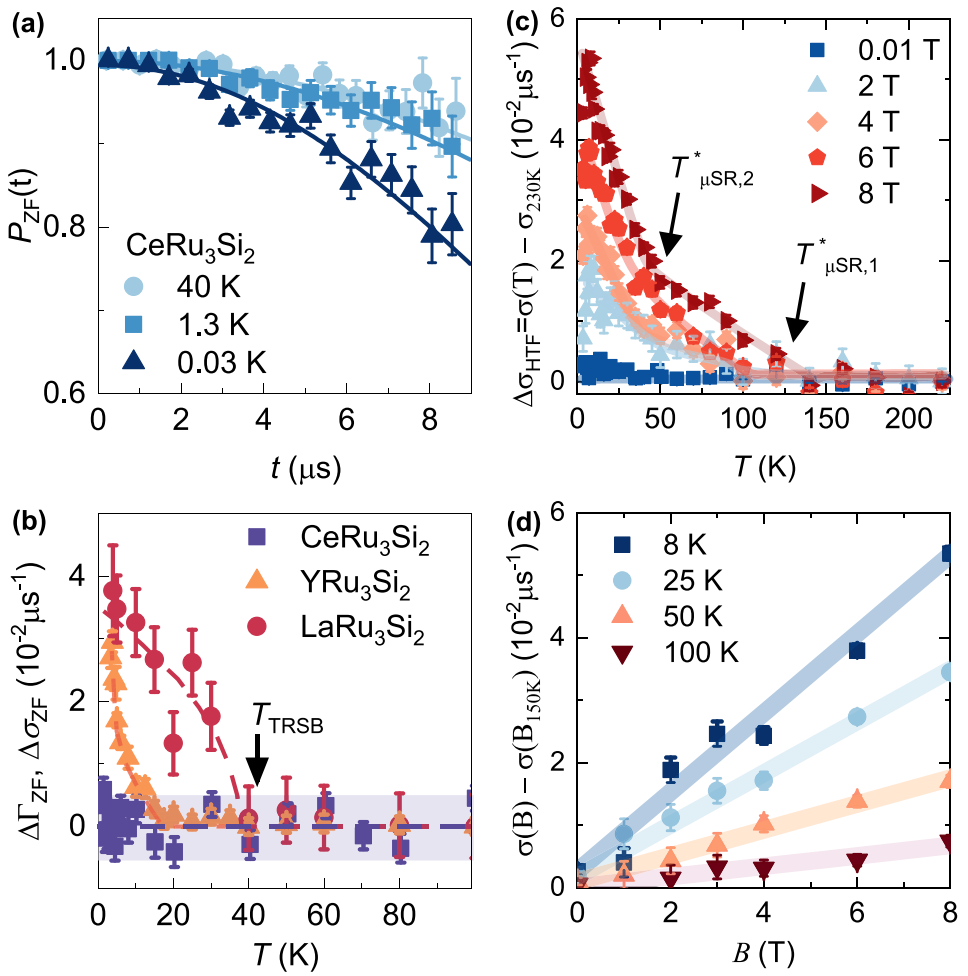


**FIGURE 4** | Zero- and high-field $\mu$ SR experiments on $CeRu_3Si_2$. (a) The ZF-$\mu$SR time spectra obtained at three different temperatures, $T$ = 0.03, 1.3, and 40 K, covering the temperature range both below and above $T_c$. The solid curves represent fits to the recorded time spectra, using the Gaussian Kubo Toyabe (GKT) function. (b) Temperature dependence of the zero-field $\mu$SR relaxation rates, $\Delta\Gamma_{ZF}$ and $\Delta\sigma_{ZF}$, shown after subtraction of the high-temperature contribution. Because the zero-field $\mu$SR spectra of the Y and La samples exhibit an exponential form, with the corresponding relaxation rate $\Gamma$ increasing at low temperatures, we present $\Delta\Gamma_{ZF}$. In contrast, the Ce sample shows Gaussian depolarization in zero field, and thus the Gaussian relaxation rate $\Delta\sigma_{ZF}$ is presented. (c) Temperature dependence of the transverse-field $\mu$SR relaxation rate $\Delta\sigma_{HTF}$, recorded under various applied magnetic fields up to 8 T, shown after subtraction of the high-temperature contribution. Arrows mark two characteristic temperatures $T^*_{\mu SR,1}$ and $T^*_{\mu SR,2}$. (d) Field dependence of $\Delta\sigma_{HTF}$ at four selected temperatures below $T_1^*$.

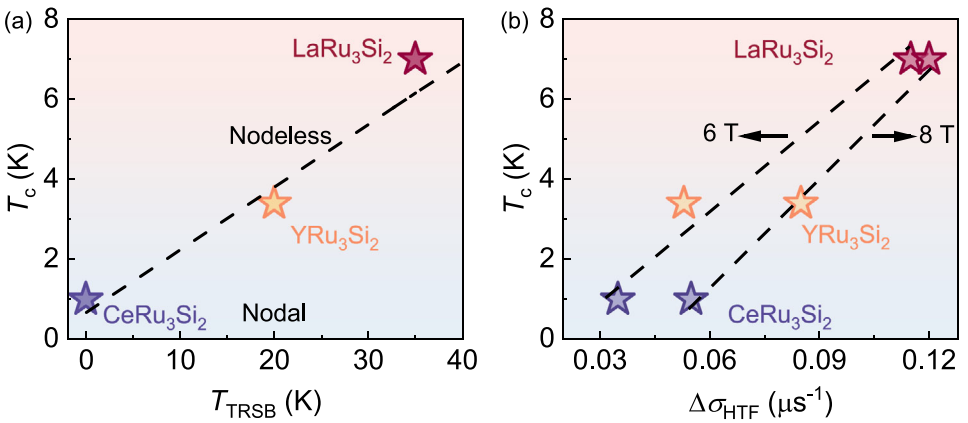


**FIGURE 5** | Scaling between superconducting and normal state properties across the $ARu_3Si_2$series ($A$ = Ce, Y, La). (a,b) Superconducting transition temperature $T_c$ plotted as a function of the zero-field normal-state TRS breaking onset temperature, $T_{TRSB}$, (a) and the absolute value of the field-induced relaxation rate measured at 6 T and 8 T (b).

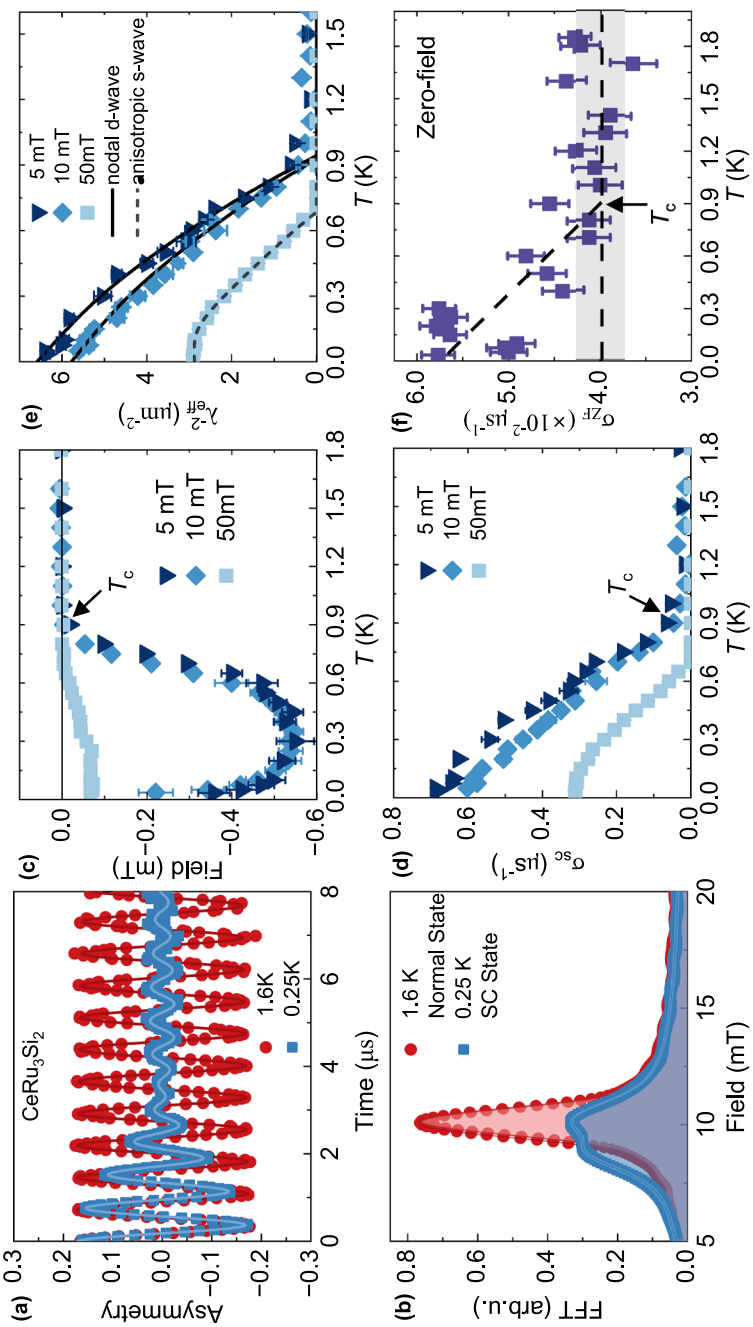


**FIGURE 6** | $\mu$SR insights into the superconducting state of $CeRu_3Si_2$. (a) Transverse-field (TF) $\mu$SR time spectra obtained above (1.6 K) and below (0.25 K) the SC transition under an applied magnetic field of 10 mT. The solid lines represent fits to the data using Equation S1 (see Supporting Information). Error bars are the standard error of the mean (s.e.m.) in about $10^6$ events. (b) Fourier transform of the measured time spectra in the normal and superconducting states. (c,d) Temperature dependence of the diamagnetic shift $\Delta B_{\text{int}}(T)$ (c) and the muon spin depolarization rate $\sigma_{\text{sc}}(T)$ (d) under the applied magnetic fields of 5, 10, and 50 mT. The error bars represent the standard deviation of the fit parameters. (e) Inverse squared effective penetration depth $\lambda_{\text{eff}}^{-2}$ as a function of temperature fitted with several theoretical models (see Supporting Information). (f) Temperature dependence of zero-field muon spin relaxation rate across $T_c$. Dashed lines are guides to the eye. The shaded region indicates the range of normal-state relaxation rates $\sigma_{\text{nm}}$, which remains constant up to 300 K.

dependences of $\sigma_{sc}$ and $\Delta B_{int}$ for applied fields of 5, 10, and 50 mT are shown in Figure 6d,c, respectively. The large diamagnetic response observed at all fields confirms the bulk nature of superconductivity. Notably, at low fields (5 and 10 mT) an additional upturn in $\Delta B_{int}$ appears below $\simeq$ 0.3 K, which is completely suppressed at 50 mT. The disappearance of this feature with increasing field indicates that it is not of magnetic origin–since a magnetic contribution would be enhanced by field-but is instead associated with intrinsic properties of the vortex state or the superconducting gap structure. A corresponding field-dependent behavior is also evident in $\sigma_{sc}$, which shows qualitatively different temperature dependence at low and high fields. To quantitatively analyze the superconducting gap structure, we calculated the temperature dependence of the superfluid density $1/\lambda^2$ (see Equation S5/S7) and fitted the data using models describing a single isotropic full gap, an anisotropic nodeless gap, and a nodal gap. The results are presented in Figure 6e. At low fields (5 and 10 mT), the data are well described by a nodal gap model, whereas at 50 mT the penetration depth clearly saturates at low temperatures and is consistent with an anisotropic nodeless gap. These results are suggestive of a field-induced crossover from nodal to nodeless superconductivity in $CeRu_3Si_2$. Fit parameters are presented in the Supporting Information (Table S5). Such nodal behavior at low magnetic fields is not unique within the 132 kagome family, as $LaRu_3Si_2$ and $YRu_3Si_2$ exhibit well-defined nodeless gaps even at low fields. A further distinction between $CeRu_3Si_2$ and its La/Y counterparts is revealed by zero-field $\mu$SR measurements: below $T_c$, the muon spin relaxation rate increases continuously by $\simeq 0.02$ $\mu s^{-1}$ (Figure 6f), corresponding to the appearance of spontaneous internal magnetic fields of order $\simeq$0.3 G. This is consistent with time-reversal symmetry-breaking in the superconducting state, while TRS remains preserved in the normal state. Alternative magnetic origins of the enhanced ZF relaxation are unlikely, as $CeRu_3Si_2$ exhibits a particularly clean nonmagnetic normal-state background. The weak Gaussian ZF-$\mu$SR relaxation above $T_c$ is consistent with a field distribution arising from nuclear moments, while the absence of Curie-like behavior in the muon Knight shift provides further evidence against localized magnetic moments, in agreement with the nonmagnetic $Ce^{4+}$ configuration. Against this weak and well-defined nuclear background, the additional ZF relaxation emerges at $T_c$, with a magnitude comparable to that reported [13, 40, 41] for several established TRS-breaking superconductors. Thus, the absence of static magnetic order or detectable local moments in the normal state, combined with the onset of additional relaxation at the superconducting transition, strongly suggests an intrinsic superconducting origin of the spontaneous internal fields and their association with TRS breaking. Taken together, the nodal superconducting gap at low fields, the field-induced crossover to a nodeless gap, the emergence of spontaneous internal fields below $T_c$, and the low superfluid density establish $CeRu_3Si_2$ as an unconventional superconductor and a unique member of the 132 kagome family.

## 3 | Summary and Outlook

By combining X-ray diffraction, magnetotransport, $\mu$SR, and first-principles calculations, we uncover a correlated and symmetry-broken normal state in $CeRu_3Si_2$, characterized by two distinct charge-ordered states, that evolves into unconventional nodal, TRS-breaking superconductivity. The following observations establish the distinct electronic character of $CeRu_3Si_2$ and reveal systematic connections between its normal-state electronic instabilities and superconducting ground state: **(1)** X-ray diffraction uncovers a dominant 1/2 charge order accompanied by a much weaker 1/3 order, both persisting at least up to room temperature. First-principles calculations reproduce the observed charge-order patterns and indicate that a relatively large Hubbard interaction ($U>$ 6 eV) for the Ce-$f$ states is required to account for the experimental observations. This finding highlights the strongly correlated nature of the dominant $q = 1/2$ charge order, accompanied by a weaker $q = 1/3$ component observed experimentally. While a 1/2 charge order has also been reported in $YRu_3Si_2$ [23] and $NdRu_3Si_2$ [31], $LaRu_3Si_2$ instead hosts [16] a 1/4 charge order below $\simeq$ 400 K and an additional 1/6 order below $\simeq$ 80 K. $CeRu_3Si_2$ thus constitutes the first kagome system exhibiting two distinct charge-ordering wave vectors already at room temperature. Taken together, these results demonstrate that the 132 kagome family provides a fertile platform for multiple competing and coexisting charge-ordered states. **(2)** First-principles calculations reveal the coexistence of Ru $d$-orbital kagome flat bands and flat bands derived from $Ce^{4+}4f$-states. The structural distortions associated with charge order are accompanied by a suppression of the density of states near the Fermi level associated with the in-plane Ru $d_{xy}$ and $d_{x2-y2}$ orbitals, which constitute the Ru-$d$ flat bands. In addition, we find that the Ce-$f$ flat bands shift toward higher energies upon the formation of the charge-ordered states. These results demonstrate that both electronic sectors participate in the formation of the charge-ordered states. Importantly, the Ce-derived electronic states and their correlations are essential for reproducing the relative energetics of the experimentally observed charge-ordered structures. To our knowledge, $CeRu_3Si_2$ represents the first kagome superconductor in which kagome-derived Ru-$d$ flat bands coexist with Ce-4$f$ flat bands, providing a distinct electronic setting for correlated quantum phenomena. **(3)** Deep within the charge-ordered phase, a finite magnetoresistance emerges below $\simeq$ 80 K and becomes strongly enhanced below $\simeq$ 30 K. This behavior is accompanied by a sign reversal of the Hall resistivity across $\simeq$ 80 K. Notably, no additional charge-order transitions are detected below this temperature, suggesting that the emergence of magnetoresistance and the Hall sign change arise from a reconstruction of the Fermi surface [42] driven by electronic or magnetic correlations rather than by a new static charge order. **(4)** Zero-field $\mu$SR measurements reveal no evidence for TRS breaking in the normal state, in sharp contrast to $LaRu_3Si_2$ and $YRu_3Si_2$. However, the application of a magnetic field induces a weak but bulk magnetic response, with an onset near $\simeq$ 130 K and a pronounced enhancement below $\simeq$ 55 K. The close correspondence between these temperature scales and the onset of magnetoresistance suggests a connection between the magnetic and electronic responses in $CeRu_3Si_2$. **(5)** Across the $ARu_3Si_2$ series ($A$ = Ce, Y, La), $T_c$ exhibits a systematic correlation with both the onset temperature of normal-state TRS breaking and the magnitude of the field-induced magnetic response. Although the limited number of compounds presently available precludes establishing a statistically robust universal scaling, the concurrent evolution of these quantities suggests a possible connection between normal-state symmetry breaking and superconductivity. **(6)** $CeRu_3Si_2$ is identified as the first 132-type kagome compound to host nodal superconductivity at low magnetic fields, coexisting with spontaneous internal magnetic fields. This provides compelling evidence for intrinsic TRS break-

ing in the superconducting state and places $CeRu_3Si_2$ at the intersection of kagome flat-band physics, strong correlations, and unconventional superconductivity. **(7)** We find an intriguing field dependence of the superconducting gap structure in $CeRu_3Si_2$, revealed by the temperature dependence of the superfluid density: at low magnetic fields (5 and 10 mT) the data are best described by a nodal gap, whereas at higher fields (50 mT) an anisotropic nodeless behavior emerges. While magnetic impurity scattering induced by Fe substitution has been associated with the emergence of nodal superconductivity in $La(Ru_{1-x}Fe_x)_3Si_2$ [18], such a mechanism is unlikely in $CeRu_3Si_2$. Ce is predominantly in the nonmagnetic $Ce^{4+}$ ($4f^0$) configuration, consistent with our $\mu$SR and magnetization measurements showing no signatures of static magnetism or localized Ce moments. In the present case, several scenarios may account for this crossover. A natural explanation is multiband superconductivity [43, 44], in which a nodal or strongly anisotropic gap on one Fermi-surface sheet dominates the low-field response but is preferentially suppressed by magnetic field due to its smaller gap magnitude or lower upper critical field, leaving a fully gapped band to govern the superfluid response at higher fields. Alternatively, the nodes may be accidental rather than symmetry protected [45], in which case magnetic field can lift deep gap minima or nodes by modifying the relative weights of competing gap harmonics or by suppressing intertwined electronic orders. In this context, field-induced suppression of competing charge-ordered or pair-density-wave correlations–known to generate nodal-like quasiparticle spectra–could restore an uniform superconducting state with a full gap. Finally, field-dependent vortex-state effects and nonlinear quasiparticle contributions may also affect the apparent low-energy excitation spectrum. Together, these scenarios highlight several possible microscopic origins of the observed nodal-to-nodeless-like evolution, including multiband superconductivity, gap anisotropy, and competing electronic correlations. Distinguishing between these possibilities will require further field-resolved spectroscopic and thermodynamic studies, as well as high-field magnetization and magneto-optical Kerr effect measurements.

In hindsight, these results establish $CeRu_3Si_2$ as a distinct kagome superconductor in which multiple charge-ordered states, kagome-derived Ru-*d* flat bands, Ce-4*f* flat bands, and unconventional superconductivity coexist. In particular, $CeRu_3Si_2$ stands out from its La- and Y-based analogues through the emergence of nodal superconductivity accompanied by spontaneous TRS breaking, establishing a qualitatively distinct superconducting ground state. At the same time, the observed correlation between $T_c$, the onset of normal-state TRS breaking, and the field-induced magnetic response provides an empirical link between the correlated, symmetry-broken normal state and superconductivity. While these observations do not establish that the different phenomena originate from a single microscopic mechanism, they provide a coherent experimental framework for exploring their possible connection. Determining the microscopic mechanism linking the normal-state electronic instabilities and unconventional superconductivity remains an important question for future investigation. Future pressure-dependent studies tracking charge order, magnetoresistance and superconductivity simultaneously will be important for resolving their microscopic relationship.

**Note added**: While preparing the revised manuscript, we became aware of a recent work [46] that independently reports charge ordering in $CeRu_3Si_2$. The charge-order structures reported therein are in good agreement with those identified in the present work.

### Author Contributions

Z.G. conceived, designed and supervised the project. Sample growth: M.S. and F.v.R.. X-ray diffraction experiments: O.G., P.K., I.B., M.S., J.O., L.M., I.P., M.v.Z., J.C. and Z.G.. Magnetotransport experiments: O.G., P.K., M.S. and Z.G. with contributions from A.S. and N.S.. Zero and high-field $\mu$SR experiments: O.G., P.K., J.G., J.A.K., T.J.H., R.K., H.L., and Z.G.. High field $\mu$SR experiments: O.G., P.K., J.N.G., A.D. and Z.G.. First-principles calculations: S.W.K. and B.M., in coordination with Z.G.. Data analysis, figure development and writing of the paper: O.G. and Z.G. All authors discussed the results, interpretation, and conclusion.

### Acknowledgements

This work was based on experiments performed at the Swiss Muon Source (S$\mu$S) Paul Scherrer Insitute, Villigen, Switzerland. Z.G. acknowledges support from the Swiss National Science Foundation (SNSF) through SNSF Starting Grant (No. TMSGI2_211750). This research was also supported by the NCCR Muoniverse, a National Centre of Competence in Research, funded by the Swiss National Science Foundation (grant number 51NF-0_229254). S.-W.K. acknowledges support from a Leverhulme Trust Early Career Fellowship (ECF-2024-052), from the research fund of Hanyang University (HY-202600000001189), and from the Nano & Material Technology Development Program through the National Research Foundation of Korea (NRF) funded by Ministry of Science and ICT (No. RS-2026-25593133). B.M. and S.-W.K. acknowledge support from a UKRI Future Leaders Fellowship [MR/V023926/1]. The computational resources were provided by the UK National Supercomputing Service ARCHER2, for which access was obtained via the UKCP consortium and funded by EPSRC [EP/X035891/1]. Z.G. acknowledges helpful discussions with PD Dr. Mark H. Fischer.

### Data Availability Statement

The data that support the findings of this study are available from the corresponding authors upon request.

### Conflicts of Interest

The authors declare no conflicts of interest.

### References

1. M. L. Kiesel and R. Thomale, "Sublattice Interference in the Kagome Hubbard Model," *Physical Review B* 86, no. 12 (2012): 121105.

2. M. Kang, S. Fang, J.-K. Kim, et al., "Twofold Van Hove Singularity and Origin of Charge Order in Topological Kagome Superconductor $CsV_3Sb_5$," *Nature Physics* 18, no. 3 (Mar 2022): 301–308, https://doi.org/10.1038/s41567-021-01451-5.

3. S.-W. Kim, H. Oh, E.-G. Moon, and Y. Kim, "Monolayer Kagome Metals $AV_3Sb_5$," *Nature Communications* 14, no. 1 (Feb 2023): 591, https://doi.org/10.1038/s41467-023-36341-2.

4. C. Lin, A. Consiglio, O. K. Forslund, et al., "Uniaxial Strain Tuning of Charge Modulation and Singularity in a Kagome Superconductor," *Nature Communications* 15, no. 1 (2024): 10466.

5. Y. Wang, H. Wu, G. T. McCandless, J. Y. Chan, and M. N. Ali, "Quantum States and Intertwining Phases in Kagome Materials," *Nature Reviews Physics* 5, no. 11 (2023): 635–658.

6. C. Mielke III, Y. Qin, J.-X. Yin, et al., "Nodeless Kagome Superconductivity in $LaRu_3Si_2$," *Physical Review Materials* 5, no. 3 (2021): 034803.

7. Z. Guguchia, C. Mielke III, D. Das, et al., "Tunable Unconventional Kagome Superconductivity in Charge-Ordered $RbV_3Sb_5$ and $KV_3Sb_5$," *Nature Communications* 14, no. 1 (2023): 153.

8. M. Jovanovic and L. M. Schoop, "Simple Chemical Rules for Predicting Band Structures of Kagome Materials," *Journal of the American Chemical Society* 144, no. 24 (2022): 10978–10991.

9. M. Kang, L. Ye, S. Fang, et al., "Dirac Fermions and Flat Bands in the Ideal Kagome Metal FeSn," *Nature Materials* 19, no. 2 (2020): 163–169.

10. O. Gerguri, D. Das, V. Sazgari, et al., "Distinct Uniaxial Stress and Pressure Fingerprint of Superconductivity in the 3D Kagome Lattice Compound $CeRu_2$," arXiv (2025): arXiv:2507.09779.

11. L. Ye, M. Kang, J. Liu, et al., "Massive Dirac Fermions in a Ferromagnetic Kagome Metal," *Nature* 555, no. 7698 (2018): 638–642.

12. H. Chen, H. Yang, B. Hu, et al., "Roton Pair Density Wave in a Strong-Coupling Kagome Superconductor," *Nature* 599, no. 7884 (2021): 222–228.

13. Z. Guguchia, R. Khasanov, and H. Luetkens, "Unconventional Charge Order and Superconductivity in Kagome-Lattice Systems as Seen by Muon-Spin Rotation," *npj Quantum Materials* 8, no. 1 (2023): 41.

14. C. Mielke III, D. Das, J.-X. Yin, et al., "Time-Reversal Symmetry-Breaking Charge Order in a Kagome Superconductor," *Nature* 602, no. 7896 (2022): 245–250.

15. Y.-X. Jiang, J.-X. Yin, M. M. Denner et al., "Unconventional Chiral Charge Order in Kagome Superconductor $KV_3Sb_5$," *Nature Materials* 20, no. 10 (2021): 1353–1357.

16. C. Mielke III, V. Sazgari, I. Plokhikh et al., "Coexisting Multiple Charge Orders and Magnetism in the Kagome Superconductor $LaRu_3Si_2$," *Advanced Materials* 37, no. 40 (2025): 2503065.

17. J. Huang, Z. Ren, H. Tan, et al., "Magnetic Field-Induced Momentum-Dependent Symmetry Breaking in a Kagome Superconductor," *Nature Physics* 22 (2026): 550–558.

18. I. Plokhikh, C. Mielke III, H. Nakamura et al., "Discovery of Charge Order Above Room Temperature in the Prototypical Kagome Superconductor $La(Ru_{1-x}Fe_x)_3Si_2$," *Communications Physics* 7, no. 1 (2024): 182.

19. K. Ma, I. Plokhikh, J. N. Graham et al., "Correlation Between the Dome-Shaped Superconducting Phase Diagram, Charge Order, and Normal-State Electronic Properties in $LaRu_3Si_2$," *Nature Communications* 16, no. 1 (2025): 6149.

20. Z. Li, S. Huyan, E. C. Thompson et al., "Superconducting Dome and Structural Changes in $LaRu_3Si_2$ Under Pressure," *Physical Review B* 111, no. 14 (2025): 144505.

21. J. Deng, Y. Jiang, T. F. Cerqueira et al., "Theory of Superconductivity in $LaRu_3Si_2$ and Predictions of New Kagome Flat-Band Superconductors," arXiv (2025): arXiv:2503.20867.

22. P. Král, V. Sazgari, Y. Ge, et al., "Uniaxial Stress-Enhanced Anisotropic Magnetoresistance and Superconductivity in the Kagome Superconductor $LaRu_3Si_2$," *Advanced Materials* (2026): e74067.

23. P. Král, J. N. Graham, V. Sazgari, et al., "Discovery of High-Temperature Charge Order and Time-Reversal Symmetry-Breaking in the Kagome Superconductor $YRu_3Si_2$," *Nature Communications* 17 (2026): 1121, https://doi.org/10.1038/s41467-025-67881-4.

24. B. Li, S. Li, and H.-H. Wen, "Chemical Doping Effect in the $LaRu_3Si_2$ Superconductor with a Kagome Lattice," *Physical Review B* 94, no. 9 (2016): 094523.

25. U. Rauchschwalbe, U. Gottwick, U. Ahlheim, H. Mayer, and F. Steglich, "Investigation of New Lanthanum-, Cerium-, and Uranium-Based Ternary Intermetallics," *Journal of the Less Common Metals* 111, no. 1–2 (1985): 265–275.

26. U. Rauchschwalbe, W. Lieke, F. Steglich, C. Godart, L. Gupta, and R. Parks, "Superconductivity in a Mixed-Valent System: $CeRu_3Si_2$," *Physical Review B* 30, no. 1 (1984): 444.

27. S. Yomo, P. Hor, R. Meng, and C. Chu, "High Pressure-Induced Anomalous Behavior in the Mixed-Valent Superconductor $CeRu_3Si_2$," *Journal of Magnetism and Magnetic Materials* 54 (1986): 477–478.

28. M. Gulácsi and Z. Gulácsi, "BCS Superconductivity in a Mixed-Valence Compound," *Solid State Communications* 90, no. 1 (1994): 51–55.

29. Y. Kishimoto, Y. Kawasaki, and T. Ohno, "Mixed-Valence State in Ce and Yb Compounds Studied by Magnetic Susceptibility," *Physics Letters A* 317, no. 3–4 (2003): 308–314.

30. O. Ivashko, F. Igoa Saldaña, J. Liu, et al., "P21.1 at PETRA III–A High-Energy X-Ray Diffraction Beamline for Physics and Chemistry," *Journal of Synchrotron Radiation* 32, no. 3 (2025): 802–814.

31. R. Misawa, S. Kitou, R. Yamada, et al., "Successive Orthorhombic Distortions in Kagome Metals by Molecular Orbital Formation," *Advanced Materials* 38 (2025): e13015.

32. S. Liu, M. Roppongi, M. Kimata, et al., "Impact of Tiny Fermi Pockets with Extremely High Mobility on the Hall Anomaly in the Kagome Metal $CsV_3Sb_5$," *Physical Review Letters* 135 (Jul 2025): 056502, https://doi.org/10.1103/d4dw-2v6k.

33. Z. Xu, T. Le, and X. Lin, "$AV_3Sb_5$ Kagome Superconductors: A Review with Transport Measurements," *Chinese Physics Letters* 42 (2025): 037304.

34. B. Mansart, M. J. Cottet, T. J. Penfold et al., "Evidence for a Peierls Phase Transition in a Three-Dimensional Multiple Charge-Density-Waves Solid," *Proceedings of the National Academy of Sciences* 109, no. 15 (2012): 5603–5608.

35. N. Ong and P. Monceau, "Anomalous Transport Properties of a Linear-Chain Metal: $NbSe_3$," *Physical Review B* 16, no. 8 (1977): 3443.

36. M. N. Ali, J. Xiong, S. Flynn et al., "Large, Non-Saturating Magnetoresistance in $WTe_2$," *Nature* 514, no. 7521 (2014): 205–208.

37. D. Qiu, C. Gong, S. Wang et al., "Recent Advances in 2D Superconductors," *Advanced Materials* 33, no. 18 (2021): 2006124.

38. K. Sedlak, R. Scheuermann, T. Shiroka, A. Stoykov, A. Raselli, and A. Amato, "Musrsim and Musrsimana: Simulation Tools for $\mu$SR Instruments," *Physics Procedia* 30 (2012): 61–64.

39. E. Brandt, "Flux Distribution and Penetration Depth Measured by Muon Spin Rotation in High-$T_c$ Superconductors," *Physical Review B* 37, no. 4 (1988): 2349.

40. V. Grinenko, S. Ghosh, R. Sarkar et al., "Split Superconducting and Time-Reversal Symmetry-Breaking Transitions in $Sr_2RuO_4$ under Stress," *Nature Physics* 17, no. 6 (2021): 748–754.

41. S. K. Ghosh, M. Smidman, T. Shang et al., "Recent Progress on Superconductors with Time-Reversal Symmetry Breaking," *Journal of Physics: Condensed Matter* 33, no. 3 (Oct 2020): 033001, https://doi.org/10.1088/1361-648X/abaa06.

42. L. Taillefer, "Fermi Surface Reconstruction in High-$T_c$ Superconductors," *Journal of Physics: Condensed Matter* 21, no. 16 (2009): 164212.

43. H.-S. Xu, Y.-J. Yan, R. Yin et al., "Multiband Superconductivity with Sign-Preserving Order Parameter in Kagome Superconductor $CsV_3Sb_5$," *Physical Review Letters* 127, no. 18 (2021): 187004.

44. W.-M. Huang and H.-H. Lin, "Pairing Mechanism in Multiband SuperConductors," *Scientific Reports* 10, no. 1 (2020): 7439.

45. I. Eremin and J. Annett, "Magnetic Field Dependence of the Superconducting Gap Node Topology in Noncentrosymmetric Ce Pt 3 Si," *Physical Reviews B* 74, no. 18 (2006): 184524.

46. R. Misawa, S. Kitou, R. Yamada et al., "Bond-Density-Wave Orders Induced by Geometric Frustration in the Kagome Metal CeRu3Si2," arXiv (2026): arXiv:2604.01691.

**Supporting Information**

Additional supporting information can be found online in the Supporting Information section.

**Supporting File:** advs78767-sup-0001-SuppMat.pdf.